Eur. Phys. J. B **51**, 29–40 (2006)
DOI: 10.1140/epjb/e2006-00190-1

THE EUROPEAN PHYSICAL JOURNAL B

Experimental study of electron-phonon properties in ZrB_2

E. Forzani[a] and K. Winzer

Erstes Physikalisches Institut, Georg-August-Universität Göttingen, 37077 Göttingen, Germany

Received 20 September 2005 / Received in final form 8 March 2006

Abstract. High quality samples and absence of superconductivity down to 40 mK make of ZrB_2 the best normal state reference system for the superconducting isostructural MgB_2. Actually, the question of pairing has to be focused on the electron-phonon interaction in the normal state. After presenting the resistivity measurements of ZrB_2, we explain the details of the Bloch-Grüneisen and Einstein models used to deduce the first results. We then compare experimental de Haas-van Alphen effect data with theoretical Fermi surfaces to present additional results on electron quasi-particle renormalization. The estimations reveal an isotropic and negligible coupling constant of in average $\langle \lambda_{tr} \rangle = 0.145$. The contribution of the coupling to the optical phonon modes is 0.082, in contrast to the known larger coupling of 0.283 [3] to the E_{2g} phonon mode in MgB_2.

PACS. 71.18.+y Fermi surface: calculations and measurements; effective mass, g factor – 71.38.-k Polarons and electron-phonon interactions – 72.10.-d Theory of electronic transport; scattering mechanisms – 74.25.Fy Transport properties

1 Introduction

The layered hexagonal diborides and their transport properties received additional attention after the discovery of superconductivity in the isostructural compound MgB_2 [1]. The superconducting state has been recently described through investigations of the electron-phonon coupling (see [2,3] and references therein). But the anomalies in MgB_2 and the origin of superconductivity can be deduced when the investigations are extended to the normal conducting diborides. Inside the class of the high temperature engineering transition metal diborides [4], we chose the ZrB_2, since we established absence of superconductivity down to 40 mK. ZrB_2 can be considered as a convenient model of the normal state properties in diborides.

We report measurements on the electron normal state of single crystal ZrB_2 and compare them to accurate lattice dynamics [5] and full potential band [6] calculations. From this, the quasi-particle renormalization due to electron-electron and electron-phonon interactions will be estimated.

2 Experimental methods

A high quality crystal of ZrB_2, 1 cm in diameter and 6 cm long, was prepared in 0.8 MPa of helium ambient gas by the RF heated floating zone method [7]. The crystal rod surface is 1 mm thick polycrystalline. Two samples free of grain boundaries were cut from the middle crystal rod using a spark erosion cutter. Their dimensions were 1.7 × 1.2 × 8.5 mm. The orientations along the major length were $[10\bar{1}0]$ and [0001], in-plane and perpendicular to the hexagonal crystal plane respectively.

The anisotropy of the resistivity was measured as a function of temperature using a four point technique. Two pairs of 0.5 mm wide nickel stripes were electrolytically plated around the samples at their ends, and copper leads were soft-soldered around the samples on to these stripes. Lowest resistance contacts are necessary for very low temperature electrical measurements as to reduce warming effects and a temperature gradient to the thermometer clamped on the CuBe sample holder. The signal voltage was measured with a lock-in amplifier in phase with the sampling current at 117 Hz. Measurements from room temperature to 4.2 K were performed travelling the sample holder in the exchange gas of a liquid helium cryostat. For the very low temperature interval measurement from 40 mK to 4.2 K the sample was mounted in a demagnetization cryostat.

Magnetization measurements of the de Haas-van Alphen (dHvA) effect were performed in a ^{3}He-cryostat for magnetic field sweeps up to 13.5 T and temperatures of 0.4–2 K. The measurements employed the field modulation method with a balanced coil magnetometer in which the sample is held. In order to study a crystallographic

---

[a] e-mail: `eforzan@gwdg.de`

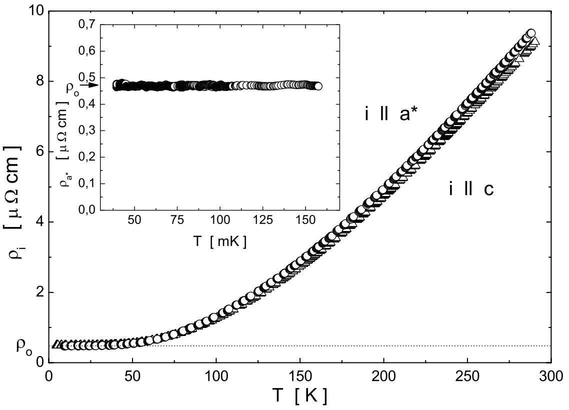

Fig. 1. Temperature dependence of the resistivity of ZrB_2 for current flow $i \parallel \mathbf{a}^* = [10\bar{1}0]$ (○) and $i \parallel \mathbf{c} = [0001]$ (Δ) down to 4.2 K (cooling curves). Inset: very low temperature resistivity about 40 mK for $i \parallel \mathbf{a}^*$ without sign of superconductivity (warming up curve).

plane the magnetometer is mounted into a one-axis cryogenic goniometer, allowing the sample-magnetometer system to be rotated about an axis normal to the magnetic field [8]. Conventional angle steps are 0.5° to 2.5°. To study the complete Fermi surface of ZrB_2, three intersecting crystallographic planes are sufficient. We chose conveniently the planes $(11\bar{2}0)$, (0001) and $(10\bar{1}0)$ and the following intervals of investigation respectively:

90° interval from $[0001]$ to $[10\bar{1}0]$
30° interval from $[11\bar{2}0]$ to $[10\bar{1}0]$
90° interval from $[11\bar{2}0]$ to $[0001]$

The sample filling the coil magnetometer should be cylindrical with dimensions $1.5 \times 1.5 \times 3$ mm, but only two samples with axis parallel to the $[0001]$ and $[11\bar{2}0]$ direction are needed to perform the three scans. The cylinders were cut with spark erosion from the samples used for the transport measurements. The axis orientation was accurately determined by x-ray-diffraction analysis. The samples were chemically polished in diluted HCl and HNO_3 solution to remove surface damages and to fit the sample holder. Reflection Laue photograph method was used to orient in the rotator the crystallographic plane to be scanned.

3 Results and discussion

3.1 Electrical resistivity

The electrical resistivities measured for current flow along the $[0001]$ and $[10\bar{1}0]$ axes show a characteristic "simple metal" temperature dependence and exhibit very little anisotropy, as shown in Figure 1. Measurements down to 40 mK showed no superconductivity, see inset in Figure 1 for the in-plane resistivity. The small residual resistivities $\rho_o \approx 0.5$ $\mu\Omega\,$cm and the large residual resistivity ratios RRR $= \rho(300\text{ K})/\rho(4.2\text{ K}) \approx 20$ indicate the high quality of the crystal samples. The maximum reported value of RRR is 25 [37].

3.1.1 The Bloch-Grüneisen model

Matthiessen rule states that the measured resistivity ρ at a given temperature T consists of the temperature-dependent resistivity $\rho(T)$ and the temperature-independent residual resistivity ρ_o as

$$\rho = \rho_o + \rho(T). \tag{1}$$

ρ_o is caused by impurities and crystal imperfections and $\rho(T)$ is due to electron scattering by lattice vibrations, when magnetic effects and/or impurities are not taken into account.

In 1930 Bloch [9] developed a theory for the lattice resistance of a pure metal as a function of temperature which led to the formula

$$\rho(T) = (m-1)\rho'\,\Theta_D \cdot \left(\frac{T}{\Theta_D}\right)^m \cdot J_m\left(\frac{\Theta_D}{T}\right) \tag{2}$$

$$J_m\left(\frac{\Theta_D}{T}\right) = \int_0^{\Theta_D/T} \frac{z^m\,dz}{(e^z-1)(1-e^{-z})} \tag{3}$$

where $m = 5$ and $J_m(x)$ is another of the class of Debye integrals [10] for specific heat [11]. The temperature depending part of the resistivity has the form of the general Bloch-Grüneisen (BG) formula

$$\rho_{BG} = (m-1)\rho'\,T \cdot \left(\frac{T}{\Theta_D}\right)^{m-1} \cdot J_m\left(\frac{\Theta_D}{T}\right) \tag{4}$$

with $m \leq 5$ and $J_m(\frac{\Theta_D}{T})$ from equation (3), which can be simplified by transformations and substitutions [12] into

$$J_m\left(\frac{\Theta_D}{T}\right) = 2^{m-1}\int_0^{\Theta_D/2T} z^{m-2}\left[\frac{z}{\sinh z}\right]^2 dz. \tag{5}$$

Integral (5) cannot be solved analytically into a tractable function but limiting curves are found. For $T > \Theta_D$, the expansion

$$\left[\frac{z}{\sinh z}\right]^2 = 1 - \frac{z^2}{3} + O\left(z^4\right) + ... \tag{6}$$

approaches rapidly 1 and equation (5) can be integrated:

$$J_m\left(\frac{\Theta_D}{T}\right) = \frac{2^{m-1}}{m-1}\left[z^{m-1}\right]_0^{\Theta_D/2T}\ , \tag{7}$$

thus equation (4) becomes

$$\rho_{BG} = \rho'\,T. \tag{8}$$

For $T \leq 0.1\ \Theta_D$, $J_m(\frac{\Theta_D}{T})$ tends to a definite numerical value j_m giving for the resistivity the Grüneisen empirical power law dependence [13]

$$\rho_{BG} = (m-1)\,j_m\,\rho'\,T \cdot \left(\frac{T}{\Theta_D}\right)^{m-1}. \tag{9}$$

The power index $m = 5$ for free-electron metals can assume values between 3 and 5 when including the quasiparticle effects, and reduces to 2 as disorder increases [14]. $m = 3$ is particularly associated to interband electron-phonon scattering [15,16].

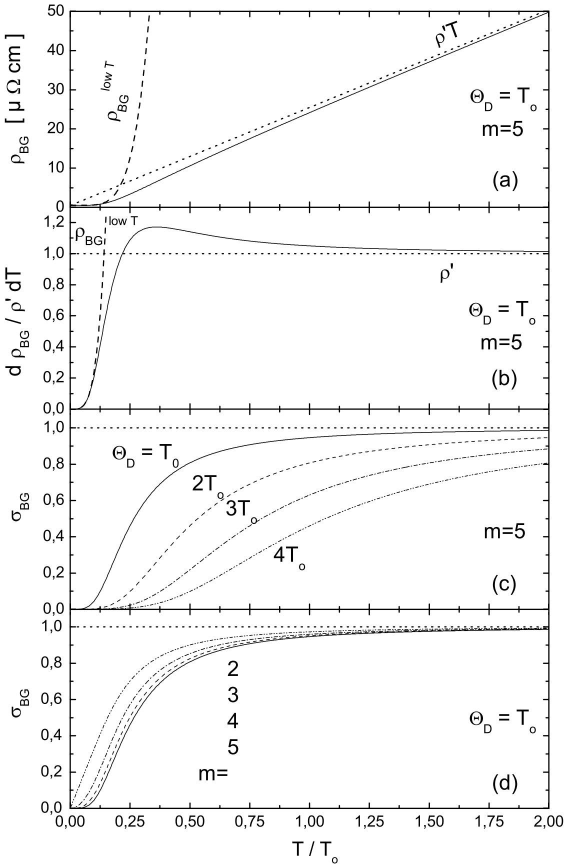

Fig. 2. Numerical solution of the BG formula as a function of reduced temperature $\frac{T}{T_o}$. (a) equation (4) (solid line) is calculated for $m = 5$, $\Theta_D = \mathrm{T}_o$ and a given ρ'. Broken lines are the limiting curves (8) and (9). (b) First derivative of the functions (4), (8) and (9), scaled to the high temperature limit ρ'. (c) equation (4) scaled to the high temperature approximation (8) (solid line) and its dependence on Debye temperature (broken lines). (d) equation (4) scaled to (8) (solid line) and its dependence on index m (broken lines).

3.1.2 Study of the BG function

The numerical solution of the integral (5) permitted to calculate the BG formula. The result as a function of temperature is shown in Figure 2a, together with the analytical limits (8) and (9). The derivative scaled to the high temperature limit is shown in Figure 2b. The numerical result of the BG formula predicts that the resistivity changes curvature at an inflection point inside the interval $\frac{\Theta_D}{4} < T < \Theta_D$. The first derivative has a maximum, which decreases to the limit ρ' for $T > \Theta_D$. These informations are necessary for a right interpretation of the measured resistivity curves. Measurements are commonly limited to temperature intervals $T \lll \Theta_D$, because of the high Debye temperatures $\Theta_D > 500$ K of the intermetallic materials. Thus measurements lie commonly in the range of maximum slope of the BG formula. When the Debye temperature is large, the maximum becomes flatter. The derivative is practically constant above $\frac{\Theta_D}{4}$ and the resistivity has a linear dependence of the temperature.

The influence of the parameters Debye temperature Θ_D and index m on the BG formula is made clear once the equation (4) is scaled to equation (8)

$$\sigma_{BG} = \frac{\rho_{BG}}{\rho' T} \tag{10}$$

and is represented as in Figures 2c and 2d.

We found similarity to the Hill sigmoid function

$$\sigma = \frac{\left(\frac{T}{\Theta_D}\right)^{m-1}}{1 + \left(\frac{T}{\Theta_D}\right)^{m-1}}. \tag{11}$$

Both are step functions of temperature with a smooth change of curvature (positive maximum of the first derivative) at the inflection point T_i^{BG} and T_i respectively. Multiplication of the maximum derivative with the inflection point value results into the dimensionless inflection factor. Inflection point and factor are temperature independent functions of Θ_D and m. The details are illustrated in Figure 3 for σ and for σ_{BG}. T_i shows a kind of direct proportionality with both Θ_D and m. The value of σ and of the inflection factor at T_i grow with m but are constant in Θ_D. It follows that increasing Θ_D (or T_i), the slope of σ at the inflection is inversely proportional to T_i. Figure 3 also shows that σ_{BG} behaves like σ only for m between 2 and 3. T_i^{BG} has in the contrast lower values so that the inflection factor gives for such values a steeper maximum slope. For m larger than 3, the inflection point T_i^{BG} behaves differently than T_i and becomes independent from m. Also the inflection factor is approximately constant with m, so that m has no influence in the actual maximum slope of σ_{BG}. The value of σ_{BG} at the inflection point reaches a local maximum for $3 < m < 4$.

3.1.3 Data interpretation with the BG model

By fitting equation (8) to the data set inside $\frac{\Theta_D}{4} < T < \Theta_D$, as is often done in the literature [3,17], the resulting value ρ' is closed to the maximum of the slope, compare Figures 2a and 2b. The resistivity curves of ZrB$_2$ in Figure 1 have a linear temperature dependence above $T \approx 225$ K, with a temperature coefficient ρ' of nearly 0.05 $\mu\Omega$ cm/K. According to the extended linearity condition $T \geq \Theta_D/4$, we obtain a very high Debye temperature $\Theta_D \approx 900$ K. As discussed in the previous Section 3.1.2, the temperature interval of the measurements is insufficient for a comparison with function (8) to be reliable.

A more precise evaluation of Θ_D follows from numerical analysis of the data on the basis of equations (4) and (5) with a fitting procedure, where the parameters are m, ρ' and Θ_D. Their physical interpretation will be developed from the electrical transport theory presented in the next Section 3.1.4. The temperature dependence of the resistivity curves was fitted in two steps to the function (1) using for $\rho(T)$ the BG limit (9) and then formula (4) with (5). The least-squares method minimizes

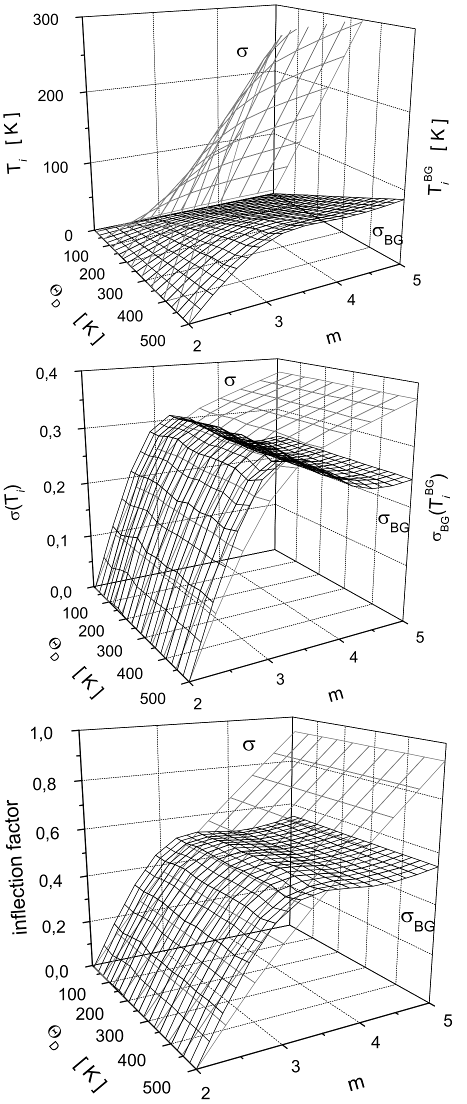

Fig. 3. σ and σ_{BG} inflection characteristics as a function of Debye temperature and index m. (from top to bottom) Inflection point T_i, function value $\sigma(T_i)$ and inflection factor of function (11) are compared with inflection point T_i^{BG}, function value $\sigma_{BG}(T_i^{BG})$ and inflection factor of function (10) respectively. (See also Fig. 2c and Fig. 2d for σ_{BG}).

the mean squared error

$$S(m,\rho',\Theta_D) = \frac{1}{N-2}\sum_k \left(\rho_{calc}(T_k) - \rho_{interp}(T_k)\right)^2 \tag{12}$$

between the calculated resistivities and the linear interpolated data values at a regular mesh of N sampling temperatures T_k. The total relative error of the best fit is

$$\bar{S}(m,\rho',\Theta_D) = \frac{1}{N-2}\sum_k \left(\frac{\rho_{calc}(T_k) - \rho_{interp}(T_k)}{\rho_{calc}(T_k)}\right)^2, \tag{13}$$

that would be zero if a true solution existed. Up to nearly 80–90 K all the curves are well fitted by the power law (9) $\rho = \rho_o + a\cdot T^m$ with $m \cong 4$, as can be seen in Figure 4. The complete data set was then fitted to (4), using the fixed $m = 4$ as to reduce the number of fitting parameters. We obtained the best fitting curves with the parameters listed in Table 1 [18]. An example is shown in Figure 5. The fits reproduce the experimental curves very well, except for deviations between 1 and 10% in the temperature interval from 50 to 150 K and above 250 K, see Figure 5b. This is due to the change of curvature in the BG curve around $\Theta/4$, as shown in Figures 2a and 2b, which is not reproduced from the data. It is clear that the BG model represents for ZrB$_2$ an approximation and other terms should be introduced with a more extended model.

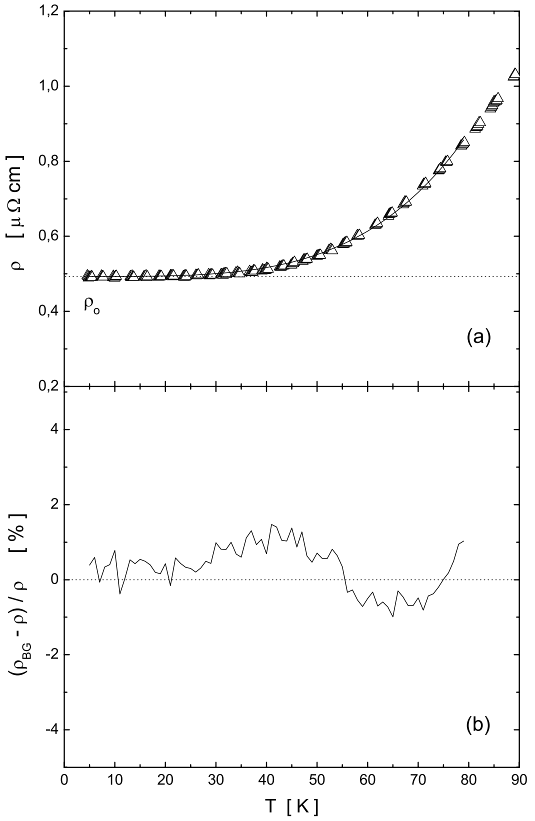

Fig. 4. Low temperature resistivity of ZrB$_2$. (a) Experimental data of Figure 1 for $\boldsymbol{i}$ || [0001] (Δ) and the fitted Bloch-Grüneisen function in the low temperature limit (9) (solid line). (b) The relative deviations of the experimental data from the fit.

Table 1. Resistivity parameters from the fitted Bloch-Grüneisen function. Values in square brakets are held constant during the fitting procedure.

Sample	EK1	EK2
resistivity	$\boldsymbol{i}$ || [0001]	$\boldsymbol{i}$ || [10$\bar{1}$0]
ρ_o [$\mu\Omega$cm]	0.493	0.475
RRR	19.51	21.03
m	[4]	[4]
ρ' [$\mu\Omega$cm/K]	0.04	0.041
Θ_D [K]	742.7	724.4
$\bar{S}$	1.844×10^{-3}	2.848×10^{-3}

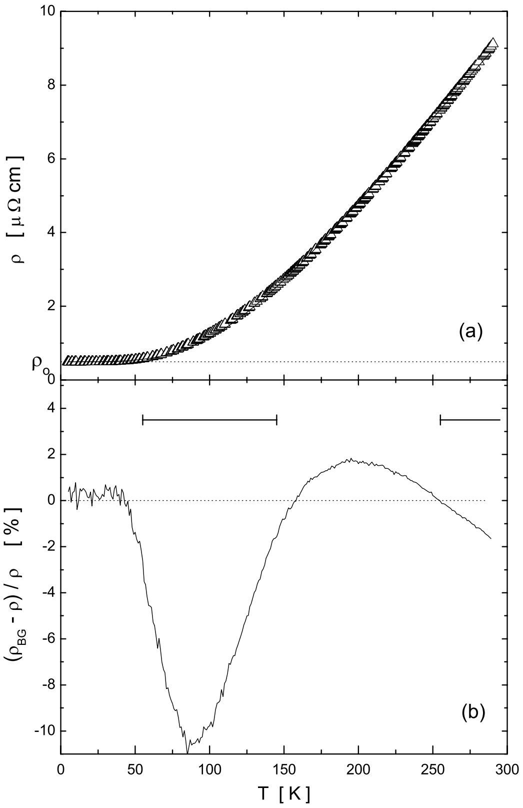

Fig. 5. Resistivity of ZrB$_2$. (a) Experimental data of Figure 1 for $i \,||\, [0001]$ (Δ) and the fitted Bloch-Grüneisen function (solid line). (b) The relative deviations of the experimental data from the fit. Intervals of maximum or growing deviation (bars).

3.1.4 The transport theory model

In the formal transport theory the kinetic method presented in [19] results in a simple expression of the electron average drift velocity

$$\langle \delta v \rangle = \frac{e\ v_x\ \tau}{\partial\epsilon/\partial v} E_x, \tag{14}$$

due to the energy gain $\partial\epsilon$ in the applied electric field E_x along a crystal direction x and for the scattering relaxation time τ. For the n electrons per unit cell, this means a current density $j_x = ne\langle\delta v\rangle$, which defines the electrical conductivity

$$\sigma = \frac{n\ e^2\ v_x\ \tau}{\partial\epsilon/\partial v} \tag{15}$$

of the macroscopic transport relation $\mathbf{j} = \sigma\ \mathbf{E}$. Equation (15) reduces to the well known relation $\frac{n\ e^2\ \tau}{m_e}$ for free electrons. Considering realistic quasi-particles energy bands $\epsilon_n(k)$, velocities $v_n(k)$ and density of states $N(\epsilon_k)$, for which

$$n = \int_0^{\epsilon_F} N(\epsilon_k)\ d\epsilon, \tag{16}$$

we obtain the general relation

$$\sigma = 2N(\epsilon_F)\left\langle v_x^2\right\rangle e^2\tau. \tag{17}$$

$N(\epsilon_F)\left\langle v_x^2\right\rangle$ is the weighted mean square velocity, averaged over the density of states for given spin-direction at the Fermi-level,

$$N(\epsilon_F)\left\langle v_x^2\right\rangle = \int_0^{v_F} N(\epsilon_k)\ v_x dv \cong \sum_k v_x^2(k)\delta(\epsilon_k - \epsilon_F) \tag{18}$$

and τ the electron relaxation time for impurity and phonon dominated scattering

$$\frac{1}{\tau} = \frac{1}{\tau^{imp}} + \frac{1}{\tau^{ep}} + ..., \tag{19}$$

both evaluated in the applied electric field E_x direction. For a complete discussion see for example [20]. Here τ^{imp} is a temperature independent term, while τ^{ep} is the temperature dependent term for the electron-phonon interaction.

F.J. Pinski, P.B. Allen and W.H. Butler [21] presented calculations in the lowest-order variational approximation (LOVA), which show the use of realistic phonons, energy bands, and matrix elements for the scattering time τ^{ep}, as opposed to traditional approximations such as the BG formula. The resulting LOVA formula for (19) is

$$\frac{1}{\tau^{ep}} = \frac{2\pi k_B T}{\hbar} 2\int_0^\infty \frac{d\omega}{\omega}\alpha^2(\omega)F(\omega)\frac{x^2}{\sinh^2 x} \tag{20}$$

with $x = \frac{\hbar\omega}{2k_BT}$, ω the phonon frequency. The integral is evaluated in terms of the transport spectral function $\alpha_{tr}^2(\omega)F(\omega)$ which is analog of the electron-phonon spectral function of the superconductivity theory [22] and defined in [23]. Therefore, after (17) and (20), the LOVA expression for the electrical resistivity is

$$\rho^{ep} = \frac{2\pi k_B T}{\hbar N(\epsilon_F)\left\langle v_x^2\right\rangle e^2}\int_0^\infty \frac{d\omega}{\omega}\alpha_{tr}^2(\omega)F(\omega)\frac{x^2}{\sinh^2 x}, \tag{21}$$

which is also known as Boltzmann equation. By analogy with the superconducting notation, the parameter λ_{tr} is defined as follows

$$\lambda_{tr} = 2\int_0^\infty \frac{d\omega}{\omega}\alpha_{tr}^2(\omega)F(\omega). \tag{22}$$

The parameter λ_{tr} is the transport analog of the dimensionless parameter λ which determines the superconducting transition temperature T_c [23].

In the high temperature (small x) limit the series expansion of $\frac{x^2}{\sinh^2 x}$ is conveniently used in equation (20)

$$\frac{1}{\tau^{ep}} = \frac{2\pi k_B T}{\hbar} 2\int_0^\infty \frac{d\omega}{\omega}\alpha^2(\omega)F(\omega) \times\left[1 - \frac{1}{3}\left(\frac{\hbar\omega}{2k_BT}\right)^2 + ...\right] \tag{23}$$

and again by analogy to (22) we introduce the definition

$$\lambda_{tr}\left\langle\omega^n\right\rangle_{tr} = 2\int_0^\infty d\omega\omega^{n-1}\alpha_{tr}^2(\omega)F(\omega). \tag{24}$$

$\langle \omega^n \rangle_{tr}$ is a weighted mean phonon frequency at the nth order. It follows that at high temperatures equation (20) and equation (21) become respectively

$$\frac{1}{\tau^{ep}} = \frac{2\pi k_B T}{\hbar}\,\lambda_{tr}\left[1 - \frac{\hbar^2 \langle \omega^2 \rangle_{tr}}{12 k_B^2 T^2} + ...\right] \tag{25}$$

$$\rho^{ep} = \frac{2\pi k_B T}{2\hbar N(\epsilon_F)\,\langle v_x^2 \rangle\, e^2}\,\lambda_{tr}\left[1 - \frac{\hbar^2 \langle \omega^2 \rangle_{tr}}{12 k_B^2 T^2} + ...\right]. \tag{26}$$

Considering that a typical phonon energy $k_B \Theta_D = \hbar \omega_D$ leads in the LOVA procedure to the identification $\omega_D^2 = \frac{3}{2}\langle \omega^2 \rangle_{tr}$, we found a relation for the high temperature interval $T \geq \frac{\Theta_D}{2}$. For these temperatures all the terms in the expansion can be neglected and equations (25) and (26) reduce to a linear temperature dependence

$$\frac{1}{\tau^{ep}} = \frac{2\pi k_B T}{\hbar}\,\lambda_{tr} \tag{27}$$

$$\rho^{ep} = \frac{2\pi k_B T}{2\hbar N(\epsilon_F)\,\langle v_x^2 \rangle\, e^2}\,\lambda_{tr}. \tag{28}$$

Equation (28) is a modern version of the equations (2) or (4) derived earlier by Bloch. It is generalized to include realistic (nonspherical) energy bands, phonons and electron-phonon matrix elements but it is based on a model employing Debye phonons, a spherical Fermi surface and deformation-potential electron-phonon coupling via longitudinal phonons only, with no umklapp scattering [21]. Thus, assuming a spherical Fermi surface, the factor $v_x^2(k)$ in equation (18) can be replaced by a constant v_F^2. The integrals that conduct to the transport spectral function result in the Debye approximation

$$\alpha_{tr}^2(\omega) F_D(\omega) = 2\lambda_D \left(\frac{\omega}{\omega_D}\right)^4 \Theta(\omega_D - \omega), \tag{29}$$

where ω_D is the Debye frequency, $\lambda_D \approx \lambda_{tr}$. The step function $\Theta(\omega_D - \omega)$ is equal to unit for $0 < \omega < \omega_D$ and zero outside. For a comparison of equation (29) with real spectral functions see [21].

Using the spectral function (29), the expression for the resistivity (21) becomes

$$\rho_D = \frac{2\pi k_B T}{\hbar N(\epsilon_F)\,\langle v_x^2 \rangle\, e^2}\int_0^{\omega_D} \frac{d\omega}{\omega}\,\frac{x^2}{\sinh^2 x}\,2\lambda_{tr}\left(\frac{\omega}{\omega_D}\right)^4. \tag{30}$$

Elementary substitutions [24] transform it into

$$\rho_D = \frac{2\pi k_B T}{2\hbar N(\epsilon_F)\,\langle v_x^2 \rangle\, e^2}\lambda_{tr}\; 4\left(\frac{T}{\Theta_D}\right)^4 2^4 \int_0^{\frac{\Theta_D}{2T}} x^3 \frac{x^2}{\sinh^2 x}\,dx, \tag{31}$$

which reproduces equation ρ_{BG} in (4) for $m = 5$, thus giving an expression for the temperature coefficient

$$\rho' = \frac{2\pi k_B}{2\hbar N(\epsilon_F)\,\langle v_x^2 \rangle\, e^2}\,\lambda_{tr}. \tag{32}$$

Although equation (31) for the resistivity is based on a highly simplified model, it captures the correct trends of the temperature dependence and, considering equation (28), reproduces the LOVA calculated result in the high temperature limit

$$\rho^{ep} \cong \rho_D = \rho_{BG} = \rho' \, T. \tag{33}$$

The electrical resistivity of a crystalline metal is related to the quasi-particle transport scattering rate $\frac{1}{\tau}$ and the Drude plasma frequency Ω_p with

$$\rho = \frac{1}{\epsilon_0\, \Omega_p^2\, \tau}, \tag{34}$$

according to the Drude relation [25]. Considering ρ to stand for the lattice resistance $\rho(T)$, $\frac{1}{\tau}$ can then be related to the transport electron-phonon coupling parameter λ_{tr} through the high-temperature expansion (25), thus leading in the linear region [17] to

$$\rho(T) = \frac{2\pi k_B T}{\hbar\, \epsilon_0\, \Omega_p^2}\lambda_{tr} \tag{35}$$

and in general after (33) to

$$\rho' = \frac{\partial \rho}{\partial T} = \frac{2\pi k_B}{\hbar\, \epsilon_0\, \Omega_p^2}\lambda_{tr}. \tag{36}$$

As seen in the numerical analysis of Section 3.1.2, considering this equation in the range $T > \frac{\Theta_D}{4}$, the first derivative approximates ρ' of equation (8) and also the constant λ_{tr} at an upper limit. But if the plasma frequency Ω_p is known from energy-band theory calculations or optical measurements, equation (36) can be introduced in equation (4) and used in the least-squares method 3.1.3 to obtain from an experimental curve of ρ empirical values of Debye temperature and electron-phonon coupling constant as fitting parameters.

If the material is superconducting, the resulting λ_{tr} may then be compared with a value for λ obtained from the experimental T_c according to the McMillan equation [23]

$$T_c = \frac{\Theta_D}{1.45}\;\exp\left(-\frac{1.04(1+\lambda)}{\lambda - \mu^*(1 + 0.62\lambda)}\right). \tag{37}$$

Θ_D is the Debye temperature and μ^* is the Coulomb pseudopotential strength representing a repulsive electron-electron interaction.

3.1.5 Developing the model: optical-phonons contribution

Since ZrB_2 has more than one atom per unit cell, it is likely that an additional scattering due to highly energetic optical mode phonons [26] occurs, which causes the steady departure of the data from the Bloch-Grüneisen behaviour. To take the optical-phonon contribution explicitly into account [3,27,28], the transport spectral function of the general Boltzmann expression for the resistivity (21) is extended to

$$\alpha_{tr}^2(\omega) F(\omega) = \alpha_{tr}^2(\omega) F_D(\omega) + \alpha_{tr}^2(\omega) F_E(\omega), \tag{38}$$

thus distinguishing the acoustic and optical phonon dominated scattering

$$\frac{1}{\tau^{ep}} \cong \frac{1}{\tau_D} + \frac{1}{\tau_E}, \tag{39}$$

because of the assumption that the contributions from acoustic and optical modes are additive (Matthiessen rule). The first term of (38) is the Debye approximation (29) which gives the BG equation (31), the second term represents the Einstein approximation

$$\alpha_{tr}^2(\omega) F_E(\omega) = \frac{1}{2}\lambda_E\ \omega_E\ \delta(\omega - \omega_E), \tag{40}$$

with ω_E a characteristic Einstein phonon frequency, λ_E the electron-phonon coupling constant for the Einstein phonons and $\delta(\omega - \omega_E)$ a delta-function at $\omega = \omega_E$. For a comparison with the complete spectral function, see [29].

In analogy with (30), the optical mode term of the resistivity becomes

$$\rho_E = \frac{2\pi k_B T}{\hbar N(\epsilon_F)\left\langle v_x^2\right\rangle e^2}\int_0^{\omega_{max}} \frac{d\omega}{\omega}\frac{x^2}{\sinh^2 x}\frac{1}{2}\lambda_E \omega_E \delta(\omega - \omega_E). \tag{41}$$

The resistivity formula can be easily written [30] as

$$\rho_E = \frac{2\pi k_B T}{2\hbar N(\epsilon_F)\left\langle v_x^2\right\rangle e^2}\lambda_E \frac{\left(\frac{\Theta_E}{2T}\right)^2}{\sinh^2\left(\frac{\Theta_E}{2T}\right)}, \tag{42}$$

which we call the Einstein formula. For high temperatures we substituted the last term with the series expansion (6). At $T > \Theta_E$ equation (42) is a linear function

$$\rho_E = \rho'_E T \quad \text{with} \quad \rho'_E = \frac{2\pi k_B}{2\hbar N(\epsilon_F)\left\langle v_x^2\right\rangle e^2}\lambda_E. \tag{43}$$

For a comparison with the BG formula see Figure 6a. At intermediate temperatures the second order term of the expansion must be considered and the resistivity can be approximated with

$$\rho_E = \rho'_E\ T\left[1 - \frac{\Theta_E^2}{12T^2}\right], \tag{44}$$

an inverse function of the type $aT - bT^{-1}$.

At very low temperatures $T < 0.1\ \Theta_E$ the terms of higher order cannot be neglected and a better approximation can be reached with the exponential representation

$$\rho_E = 2\rho'_E\ T\frac{\left(\frac{\Theta_E}{T}\right)^2}{\frac{1}{2}e^{\frac{\Theta_E}{T}} - 1}. \tag{45}$$

The limit curves and function (42) are scaled to equation (43) and represented in Figure 6c, in analogy to Figure 2c. This procedure permitted to isolate the sigmoid term dependent on the parameter Θ_E

$$\sigma_E = \frac{\left(\frac{\Theta_E}{2T}\right)^2}{\sinh^2\left(\frac{\Theta_E}{2T}\right)}. \tag{46}$$

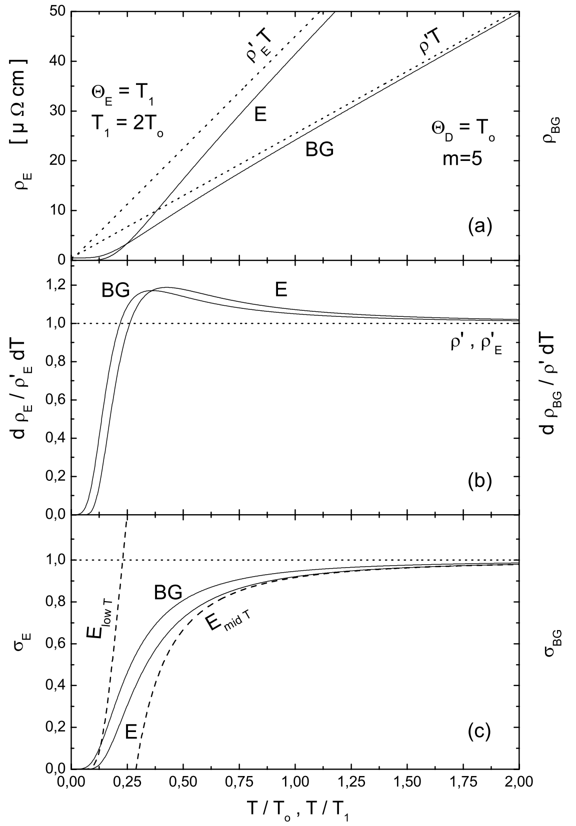

Fig. 6. The Einstein formula as a function of the reduced temperature $\frac{T}{T_1}$. (a) Comparison of equation (42) with the Bloch-Grüneisen function of Figure 2 for $m = 5$, $\rho'_E = \rho'$, $\Theta_E = 2\Theta_D$ (solid lines). Dotted lines are the high temperature limiting curves (43) and (8). (b) First derivative of the functions (42) and (4) scaled to ρ'_E and ρ' respectively, the high temperature limits. (c) equation (42) scaled to the high temperature approximation (43) in analogy to function (10) (solid lines). The Einstein term is also compared to the approximating functions (44) and (45) for middle-high and low temperature range (dashed lines).

Figure 7 shows the characteristics of σ_E and can be compared to Figure 3 for the Bloch-Grüneisen. The inflection point T_i^E increases more rapidly with the temperature parameter, also see Figure 6c. The value of σ_E and of the inflection factor at T_i^E are constant and comparable to the constant values of σ_{BG} for $m > 3$. It follows that the inflection factor gives for the physically significant interval $\Theta_E > \Theta_D$ a smaller slope at the inflection point, except for $m \approx 2$. The use of the spectral function (38) leads with relations (39), (34) and (35) to very important relations

$$\rho^{ep} \cong \rho_{BG} + \rho_E \tag{47}$$

$$\lambda_{tr} \cong \lambda_D + \lambda_E = \frac{\hbar\ \epsilon_0\ \Omega_p^2}{2\pi k_B}(\rho' + \rho'_E). \tag{48}$$

Thus considering the composition of the two formulas (4) and (42) for the resistivity, one can obtain the total electron-phonon coupling by summation of the single terms.

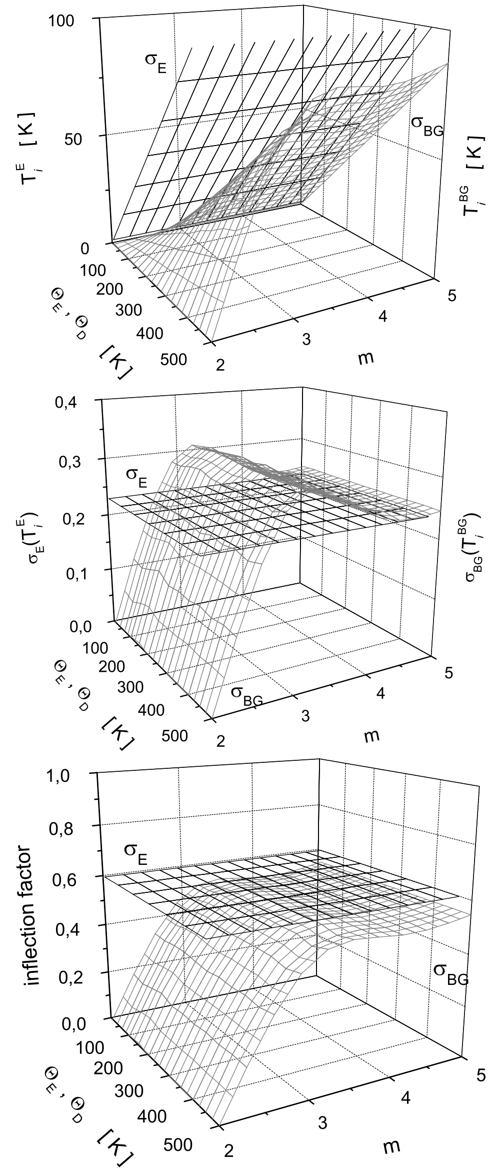

Fig. 7. σ_E inflection characteristics as a function of Einstein temperature. (from top to bottom) Plots for the inflection point T_i^E, function value $\sigma_E(T_i^E)$ and inflection factor of the function (46) are compared with the characteristics of σ_{BG}, see Figure 6c. The representation agrees with Figure 3, although σ_E does not depend on the index m.

3.1.6 Data interpretation with the transport model

The calculated spectral function [5] represented in Figure 8 shows a separated high contribution of optical phonons to the spectrum of ZrB_2, which is inconsistent with the Debye approximation (29) up to the Debye temperature as the cutoff frequency of the acoustic modes.

The optical phonon part can be easily represented by a delta function so that the Einstein contribution (42) must now be taken into account. The resistivity data are analysed using the expression (1) extended with (47) to

$$\rho = \rho_o + \rho_{BG} + \rho_E. \tag{49}$$

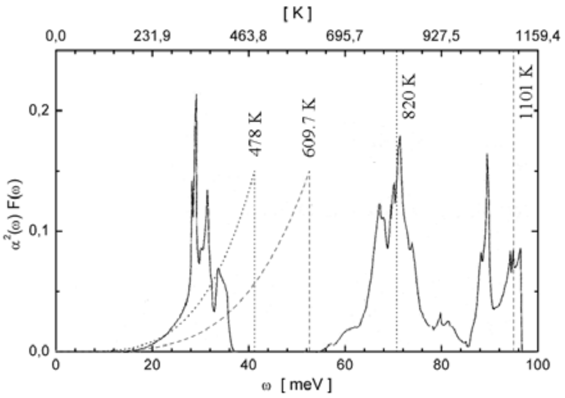

Fig. 8. Calculated electron-phonon spectral function of ZrB_2 [5]. Broken curves are Debye (29) and Einstein (40) approximations of the realistic spectral function for some of the characteristic temperatures Θ_D, Θ_E listed in Table 2.

Equation (49) is fitted to the data using the previous least-squares method for the Bloch-Grüneisen formula. Fitting parameters are now ρ', Θ_D, ρ'_E, Θ_E, while $m = 4$ is fixed. We obtained the best fitting curves with the parameters listed in Table 2. An example is shown in Figure 9. The fitting is considerably improved in comparison to the previous calculation for Figure 5, which refers to the same wide temperature range.

The obtained $\Theta_D \approx 610$ K in this approximation is less than the estimation from a simple Bloch-Grüneisen approximation, and is closer to 478 K obtained from the specific heat measurement of one sample of the same crystal [41]. However, the latter is a more reasonable value for a Debye temperature representing the cutoff energy for the acoustic phonons of ZrB_2 after Figure 8.

3.1.7 Rigid-fitting

The deviations are equally distributed on the fitted values, thus it is straightforward to take as constant those parameters, for which reliable values are known. It helps to reduce the number of fitting parameters.

Different sets of fixed parameters are listed with the results for the free parameters in Table 2. Their curves are represented in Figure 9. Actually, a very good fit is obtained for the Debye temperature fixed to the value from specific heat and the Einstein temperature fixed to 820 K, the value of the high peak of the optical phonons, Figure 8 (dotted lines).

3.1.8 Total electron-phonon coupling constant in ZrB_2

Optical measurements and local density approximation (LDA) calculations give for the plasma frequency $\hbar\Omega_p$ of ZrB_2 values between 3.16 eV and 4.1 eV [31]. Thus λ_D and λ_E estimated from equation (48) are in average 0.059 and 0.082 respectively for the [0001]-direction coupling, giving a total coupling constant of 0.141. For the in-plane coupling we estimate $\lambda_D = 0.066$ and $\lambda_E = 0.082$, giving

Table 2. Resistivity parameters from the fitted Bloch-Grüneisen-Einstein function. Values in square brakets are held constant during the fit.

sample	EK1					EK2		
m	[4]					[4]		
ρ' [$\mu\Omega\,\mathrm{cm/K}$]	0.029	0.018	0.026	0.021	0.032	0.02	0.027	0.022
Θ_D [K]	609.7	[478]	602.5	[478]	615.4	[478]	588	[478]
ρ'_E [$\mu\Omega\,\mathrm{cm/K}$]	0.018	0.025	0.016	0.027	0.017	0.025	0.015	0.027
Θ_E [K]	1101	[820]	[820]	959.3	1179	[820]	[820]	959
$\bar{S}$	4.54×10^{-5}	3.29×10^{-4}	4.6×10^{-4}	1.3×10^{-3}	2.94×10^{-5}	1.84×10^{-4}	7.52×10^{-4}	7.08×10^{-3}

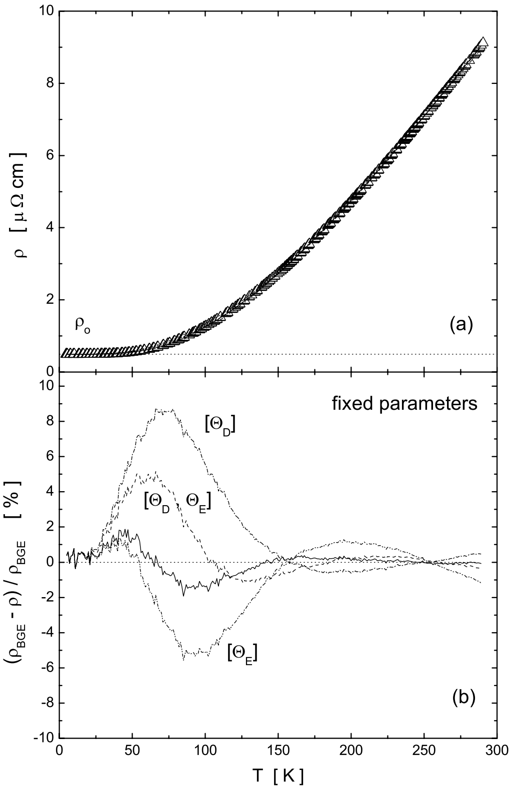

Fig. 9. Resistivity of ZrB$_2$. (a) experimental data for $i \parallel [0001]$ (Δ) and the fitted functions with the Bloch-Grüneisen and the Einstein term (solid lines). (b) The relative deviations of the experimental data from the fits. The broken lines refer to fits with different set of fixed parameters, which values are reported in Table 2. The solid line instead refers to the fit with no fixed parameters, except for $m = 4$. See also Figure 5 for comparison.

a total coupling constant of 0.148. The values for the temperature coefficients used in equation (48) result from the rigid-fitting. In the contrast, λ_D and λ_E for the in-plane coupling of MgB$_2$ are estimated in [3] as 0.075 and 0.283, giving a larger total coupling constant of 0.36.

Introducing the total mean value $\lambda_{tr} = 0.141$ or 0.148, as estimation for λ, and $\Theta_D = 478$ K in the McMillan formula (37) we find, assuming a standard value of $\mu^* = 0.10$, that the superconducting transition temperature should be in the order of pK. This conclusion is confirmed by the observed lack of superconductivity above 40 mK. The transport value for MgB$_2$ [3] instead would predict reasonably the T_c on the order of K.

Moreover, the in-plane λ_E of ZrB$_2$ quantifies the coupling to the out-of-plane vibration of the boron atoms B_{1g} and to the relative vibrations of the zirconium and boron sublattices A_{2u}, E_{1u}. The in-plane boron vibration mode E_{2g} forms the peak at the highest frequency and does not contribute to the λ_E [5,32,33]. The larger λ for the Einstein phonon indicates a dominant contribution of the optical phonons in the total electron-phonon coupling, but not of the E_{2g} mode. The E_{2g} mode of MgB$_2$ is in the contrary softened to lower energies and gives a very large contribution in the same intermediate region of the optical peak of ZrB$_2$ [32]. The coupling to the E_{2g} mode in MgB$_2$ is alone a factor 4 larger than the coupling to the optical mode in ZrB$_2$. These two aspects can be considered as the substantial differences of MgB$_2$ from ZrB$_2$ and the diborides, explaining the necessary conditions for the superconductivity in the simple layered system.

3.2 The de Haas-van Alphen effect

dHvA frequencies for the different crystal orientations in magnetic field were deduced from fast Fourier transform (FFT) spectra of the dHvA oscillations as a function of the inverse field $1/B$ at fixed temperature (400 mK) according to equation (50) (an example in Fig. 10). The cyclotron mass m^* for each extremal Fermi sheet was obtained from the amplitudes of the corresponding FFT peak by equal field scans (8–11 T) at different temperatures (0.4–1.5 K).

3.2.1 The Lifshitz-Kosevich theory

The dHvA effect is the oscillatory variation of the magnetization M of the conduction electrons with the magnetic induction B and can be expressed for one extremal Fermi sheet and no higher dHvA harmonics [34,35] as

$$M = A(B,T,T_D)\,\sin\left(\frac{2\pi F}{B} + \varphi\right) \tag{50}$$

$$A(B,T,T_D) = A_0(B,T_D)\,\frac{b\,m^* T/B}{\sinh(b\,m^* T/B)} \tag{51}$$

$$A_0(B,T_D) = m(B)\,e^{-\frac{b\,m^* T_D}{B}}\cos\left(\frac{\pi}{2} g\,m^*\right) \tag{52}$$

$$m(B) = -\left(\frac{e}{\pi}\right)^{\frac{5}{2}}\frac{F\,V}{m^*\,m_0}\left(\frac{B}{2\hbar}\right)^{\frac{1}{2}}\left(\frac{\partial^2 A_{ex}}{\partial k^2_{\|\boldsymbol{B}}}\right)^{-\frac{1}{2}}. \tag{53}$$

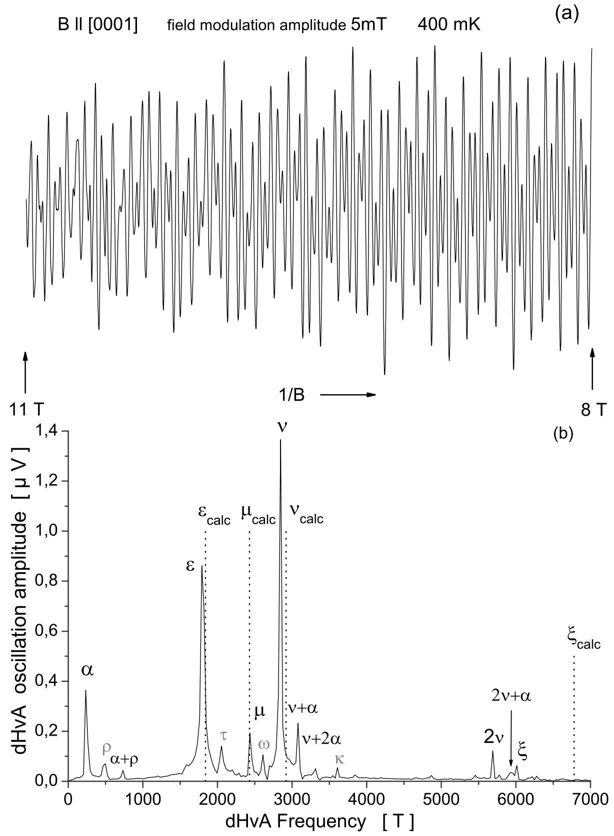

Fig. 10. dHvA oscillation in ZrB_2. (a) dHvA signal from Fermi sheets parallel to the (0001)-plane. (b) FFT of the data compared with calculated frequencies [6].

b has the value 14.69 TK^{-1} and φ is a phase constant; F, A_{ex}, m^*, T_D are the dHvA frequency, the Fermi sheet area, the enhanced cyclotron mass in unit of free-electron mass m_0 and the Dingle temperature of the extremal Fermi sheet under consideration.

3.2.2 Data analysis

Equation (51) can be rewritten as

$$\ln\left[\frac{A}{T}\left(1-e^{-2\,m^*t}\right)\right]=\ln A_0-m^*t \quad \text{with} \quad t=\frac{b\,T}{B}\cdot \qquad (54)$$

This is a self-consistent formula [36] for m^* in the rescaled temperature t. Thus the measured dHvA amplitudes $A(B,T)$ and a guess value $m^*=0.5$ or 1 were inserted in the left side of equation (54) to evaluate from the slope the m^* for the following iteration step. This procedure is then repeated with the new calculated m^* until a converging value of m^* is reached. The final data follow the linear dependence very good, see Figure 11. From the dHvA frequencies F and the effective masses m^* results an effective Fermi velocity

$$v_f=\frac{\hbar}{m^*\,m_0}\sqrt{\frac{A_{ex}}{\pi}}=\frac{1}{m^*\,m_0}\sqrt{2\,\hbar eF}, \qquad (55)$$

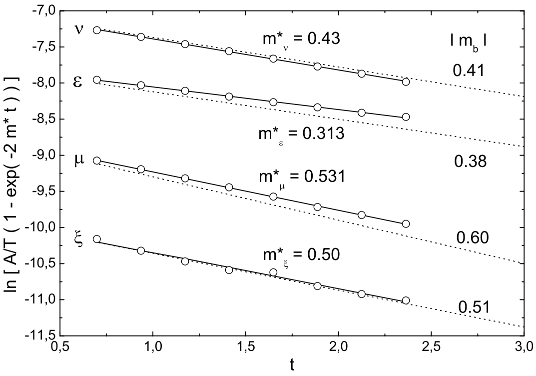

Fig. 11. Temperature dependence of the dHvA amplitudes of the fundamental oscillations for field parallel to [0001] (solid lines). The slope for each frequency gives the corresponding effective mass m^* after equation (54). The dotted lines represent the temperature dependence for the calculated band masses in [6].

the first part is a simplification for a circular Fermi sheet and the second comes from the Onsager equation $F=\hbar\,A_{ex}/2\pi e$.

3.2.3 Averaged electron-phonon coupling constant

Averaged values $\langle\lambda\rangle$ from the local electron-phonon enhancement factor $1+\lambda(\mathbf{k})$ on extremal Fermi sheets were obtained by comparing the calculated [6] band masses m_b with the dHvA cyclotron masses m^*, which include electron-phonon renormalization:

$$m^*=m_b\left(1+\langle\lambda\rangle\right). \qquad (56)$$

The results are shown in Figure 11 and Table 3. As reference we insert frequencies from other field modulation measurements [37] conduced at temperature of 1.5 K and magnetic induction up to 6 T. Under these conditions we realized that only the low frequencies (α,β) showed large amplitudes. To improve accuracy in the analysis of high frequencies and heavy masses, we extended the measurements up to 11 T and at lower temperatures down to 400 mK (Fig. 10), as demanded from the amplitude factor (51). In the plane (0001), our results for the effective masses agree with the LDA data, hinting at a negligible electron-phonon coupling or comparable with the small measurement uncertainty.

4 Conclusion

Electrical transport measurements on ZrB_2 single crystals were performed accurately and analysed in the Bloch-Grüneisen approximation. Inadequacy in the interpretation of the data suggested an analysis beyond the BG

Table 3. Calculated dHvA parameters for ZrB$_2$ [6] in comparison with data of reference [37] and present work [8]. The data confirm the previous results [38].

sample	$\frac{\text{orbit}}{\text{Fermisheet}}$	F$_{[37]}$ $[kT]$	F$_{[8]}$ $[kT]$	F$_{calc\ [6]}$ $[kT]$	$m_{b\ [6]}$ $[m_e]$	$\lvert m^*\rvert_{[8]}$ $[m_e]$	$\lvert\langle\lambda\rangle\rvert_{[8]}$	$v_{f\ [8]}$ $[10^5$ m/s$]$
EK2	$\beta\vert\vert(10\bar{1}0)$	0.300	0.303 ± 0.009	0.305	0.103	-[39]	-	-
	$\beta\vert\vert(11\bar{2}0)$	0.343	0.348 ± 0.009	-	-	0.120 ± 0.005	-	9.956
	$\zeta\vert\vert(11\bar{2}0)$	4.23	4.198 ± 0.009	-	-	0.482 ± 0.007	-	8.572
EK1	$\alpha\vert\vert(0001)$	0.238	0.235 ± 0.030	-	-	- [39]	-	-
	$\epsilon\vert\vert(0001)$	1.81	1.789 ± 0.030	1.84	–0.38	0.313 ± 0.005	0.17 ± 0.01	8.613
	$\mu\vert\vert(0001)$	2.46	2.435 ± 0.030	2.43	–0.60	0.531 ± 0.005	0.12 ± 0.01	5.927
	$\nu\vert\vert(0001)$	2.84	2.845 ± 0.030	2.92	–0.41	0.430 ± 0.004	0.05 ± 0.01	7.913
	$\xi\vert\vert(0001)$	6.05	6.013 ± 0.030	6.78	0.51	0.50 ± 0.02	0.02 ± 0.04	9.902

approximation and an additional term had to be introduced. Anisotropic electron-phonon interactions are estimated and compared to the normal state interactions in MgB$_2$, permitting further insight into the origin of superconductivity in simple layered systems.

Furthermore, studies of the de Haas-van Alphen effect provide crucial informations about the electronic properties. From the observation of oscillatory magnetization in ZrB$_2$, the shape of the theoretical Fermi surface [6] was confirmed and the effective masses of carriers on individual Fermi sheets were determined. Then, from the deviation with the results of band-structure calculations, electron-phonon coupling of quasi-particles was estimated.

As another probe for the electron-phonon coupling in ZrB$_2$, the λ_{tr} can be obtained from the experimental value of the electronic specific-heat zero temperature coefficient γ and the band-theoretical value of the quasi-particle density of states at the Fermi energy $N(\epsilon_F)$ [40]. γ is proportional to the true quasi-particle density of states at the Fermi energy $N_\gamma(\epsilon_F)$

$$\gamma = \frac{\pi^2\ k_B^2}{3} N_\gamma(\epsilon_F)\ , \tag{57}$$

and many-body effects make $N_\gamma(\epsilon_F)$ larger than $N(\epsilon_F)$

$$1 + \lambda_\gamma = \frac{N_\gamma(\epsilon_F)}{N(\epsilon_F)}\ . \tag{58}$$

λ_γ is equal to λ_{tr} provided $N(\epsilon_F)$ is calculated from an exact quasi-particle band structure which includes all many-body effects except the electron-phonon interaction [22]. Values for $N_\gamma(\epsilon_F)$ and $N(\epsilon_F)$ of ZrB$_2$ are 0.298 eV^{-1} [41] and 0.26 eV^{-1} [6] respectively. The resulting λ_{tr} from equation (58) is as small as 0.14, comparable with the results from transport and dHvA measurements.

The estimated reliability of the empirical values for λ_{tr} and $1 + \lambda_\gamma$ is about 10–20%, so that, for small lambdas, λ_γ is a much less accurate number. Nevertheless we were able to demonstrate with three different experimental procedures (resistivity, dHvA and specific heat) consistent results of a very small electron-phonon coupling constant, smaller than 0.15. Hence, in contrast to MgB$_2$, very weak electron-phonon interactions and decoupling with the E_{2g} mode are shown to be responsible in the absence of superconductivity in ZrB$_2$ and diborides.

The authors acknowledge R. Heid and K.-P. Bohnen for the phonon calculations and S.-L. Drechsler for informations about plasma frequency. E. F. is particularly grateful to H. Rosner for a detailed explanation of the calculation of the density of states of ZrB$_2$ and the disponibility of specific heat data. He also thanks R.O. Pohl for critical discussions and R. Gezzi for advice on mathematical aspects. The experiments described here would not have been possible without the extremely high-quality single crystals made available by S. Otani, Y. Ishizawa and G. Behr. The work was supported under grant of the Göttingen Graduate School of Physics.

References

1. J. Nagamatsu, N. Nagakawa, T. Muranaka, Y. Zenitani, J. Akimitsu, Nature (London) **410**, 63 (2001)
2. M. Putti, E. Galleani d'Agliano, D. Marrè, F. Napoli, M. Tassisto, P. Manfrinetti, A. Palenzona, C. Rizzuto, S. Massidda, Eur. Phys. J. B **25**, 439 (2002)
3. T. Masui, K. Yoshida, S. Lee, A. Yamamoto, S. Tajima, Phys. Rev. B **65**, 214513 (2002)
4. F. Monteverde, A. Bellosi, Adv. Eng. Mater. **6**, 331 (2004); S.C. Tjong, G. Wang, Adv. Eng. Mater. **6** 964 (2004); V. Medri, F. Monteverde, A. Balbo, A. Bellosi, Adv. Eng. Mater. **7**, 159 (2005)
5. R. Heid, K.-P. Bohnen, to be published
6. H. Rosner, J.M. An, W.E. Pickett, S.-L. Drechsler, Phys. Rev. B **66**, 024521 (2002)
7. The samples used in this work and in [41,31] are cut from the same crystal rod, for reference see: S. Otani, Y. Ishizawa, J. Crystal Growth **165**, 319 (1996)
8. E. Forzani, Master Thesis, Universität Göttingen, 2003
9. F. Bloch, Z. Phys. **52**, 555 (1929); F. Bloch, Z. Phys. **59**, 208 (1930)
10. A.V. Sologubenko, J. Jun, S.M. Kasakov, J. Karpinski, H. Rott, `cond-mat/0111273` (unpublished)
11. J.M. Ziman, *Electrons and Phonons* (Oxford, Clarendon Press 1960) pp. 357–382
12. The transformation consists in a series of substitutions applied when the Debye integral is expressed as in (3). The development of the integral (3) to

$$J_m\left(\frac{\Theta_D}{T}\right) = \int_0^{\Theta_D/T} \frac{z^m\,dz}{e^z + e^{-z} - 2}\ , \tag{59}$$

after considering that

$$\cosh z = \frac{e^z + e^{-z}}{2} \quad \text{and} \quad \sinh^2\left(\frac{z}{2}\right) = \frac{\cosh z - 1}{2}\ , \tag{60}$$

reduces into

$$\int_0^{\Theta_D/T} \frac{z^m}{2^2}\frac{dz}{\sinh^2\left(\frac{z}{2}\right)} = \int_0^{\Theta_D/T} z^{m-2}\left[\frac{\frac{z}{2}}{\sinh\frac{z}{2}}\right]^2 dz\ . \tag{61}$$

Using $\frac{z}{2}$ as integration variable, $J_m(\frac{\Theta_D}{T})$ assumes the form in equation (5)

13. E. Grüneisen, Handb. d. Phys. **XIII**, 18
14. X.H. Chen, Y.S. Wang, Y.Y. Xue, R.L. Meng, Y.Q. Wang, C.W. Chu, Phys. Rev. B **65**, 024502 (2001) and references therein
15. M. Mott, Proc. Phys. Soc. **47**, 571 (1935)
16. A. Wilson, Proc. Roy. Soc. A **167**, 580 (1938)
17. I.I. Mazin, O.V. Dolgov, Phys. Rev. B **45**, 2509 (1992)
18. This approach was applied to MgB_2 in [2]: sintered bulk MgB_2 shows a Θ_D of 1050 K and $\acute{\rho}$ of 4.9×10^{-1} $\mu\Omega$ cm/K.
19. J.M. Ziman, *Electrons and Phonons* (Oxford, Clarendon Press 1960), pp. 257-264
20. N.W. Ashcroft, N.D. Mermin, *Solid State Physics* (Holt-Saunders International Editions, 1981), pp. 244–251
21. F.J. Pinski, P.B. Allen, W.H. Butler, Phys. Rev. B **23**, 5080 (1981)
22. D.J. Scalapino, in *Superconductivity*, edited by R.D. Parks (M. Dekker, New York, 1969), Vol. 1, pp. 449–500
23. W.L. McMillan, Phys. Rev. **167**, 331 (1968)
24. The substitution in (30) of the integration variable $\omega \to x = \frac{\hbar\omega}{2k_BT}$ and the introduction of the Debye frequency $\omega_D = \frac{k_B}{\hbar}\Theta_D$ produces the resistivity formula (31)
25. T.I. Jeon, D. Grischkowsky, Phys. Rev. L **78**, 1106 (1997)
26. C.N. King, H.C. Kirsh, T.H. Geballe, Solid State Comm. **9**, 907 (1971)
27. Method adopted to transport measurements at single-crystal MgB_2 in [3]
28. P.B. Allen, W.W. Schulz, Phys. Rev. B **47**, 14434 (1993)
29. P.B. Allen, R.C. Dynes, Phys. Rev. B **12**, 905 (1975)
30. After writing the integration variable of (41) explicitely, $\omega = \frac{2k_BT}{\hbar\omega}x$, and introducing the Einstein frequency as $\omega_E = \frac{k_B}{\hbar}\Theta_E$, the use of the relation $\delta(kx) = \frac{1}{|k|}\delta(x)$ transforms the delta function into

$$\delta(\omega-\omega_E) = \frac{\hbar}{2k_BT}\delta\left(x - \frac{\Theta_E}{2T}\right)\ . \tag{62}$$

Considering that

$$\int_{-\infty}^{+\infty} f(x)\delta(x-a)dx = f(a) \text{ with } -\infty < a < +\infty\ , \tag{63}$$

the resistivity formula reduces to (42)

31. S.-L. Drechsler, private communications
32. K.-P. Bohnen, R. Heid, B. Renker, Phys. Rev. L **86**, 5771 (2001) and references therein
33. K. Kunc, I. Loa, K. Syassen, R.K. Kremer, K. Ahn, J. Phys.: Cond. Matter **13**, 9945 (2001)
34. D. Shoenberg, *Magnetic oscillations in metals* (Cambridge, 1984)
35. For a complete treatise see Chapter 2 and 3 in [8]
36. For all our experiments we found that $0.3 < m^*t < 1.2$, with $m^* \approx 0.5$ and $\langle B\rangle = 9.3$ T, so that the exponential term in equation (54) cannot be neglected. On the contrary, if $e^{-2\,m^*t} \ll 1$, the direct plot of $\ln(A/T)$ against T/B would give immediately a straight line of slope $-bm^*$
37. Results from: T. Tanaka, Y. Ishizawa, E. Bannai, S. Kawai, Solid State Comm. **26**, 879 (1978). For the technique see also: Y.Ishizawa and T. Tanaka, Inst. Phys. Conf. Ser. No. 75, 29 (1986)
38. S.-L. Drechsler, H. Rosner, J.M. An, W.E. Pickett, V.D.P. Servedio, T. Mishonov, E. Forzani, K. Winzer, J. Low Temp. Phys. **131**, 1175 (2003)
39. The amplitudes of the α and β frequencies show nearly no temperature dependence at our low temperatures. This behaviour is caused by the very small effective masses $m^*_{\alpha,\beta}$. The scattering of the data prevent any evaluation of $m^*_{\alpha,\beta}$
40. B.A. Sanborn, P.B. Allen, D.A. Papaconstantopoulos, Phys. Rev. B **40**, 6037 (1989)
41. H. Rosner, *private communications*